The Astrophysical Journal, 706:497–507, 2009 November 20 doi:10.1088/0004-637X/706/1/497

RADIATIVE MODELS OF SGR A* FROM GRMHD SIMULATIONS

Monika Mościbrodzka[1], Charles F. Gammie[1,2], Joshua C. Dolence[2], Hotaka Shiokawa[2], and Po Kin Leung[2]
[1] Department of Physics, University of Illinois, 1110 West Green Street, Urbana, IL 61801, USA; mmosc@illinois.edu
[2] Astronomy Department, University of Illinois, 1002 West Green Street, Urbana, IL 61801, USA
Received 2009 July 30; accepted 2009 October 6; published 2009 November 2

ABSTRACT

Using flow models based on axisymmetric general relativistic magnetohydrodynamics simulations, we construct radiative models for Sgr A*. Spectral energy distributions (SEDs) that include the effects of thermal synchrotron emission and absorption, and Compton scattering, are calculated using a Monte Carlo technique. Images are calculated using a ray-tracing scheme. All models are scaled so that the 230 GHz flux density is 3.4 Jy. The key model parameters are the dimensionless black hole spin a_*, the inclination i, and the ion-to-electron temperature ratio T_i/T_e. We find that (1) models with $T_i/T_e = 1$ are inconsistent with the observed submillimeter spectral slope; (2) the X-ray flux is a strongly increasing function of a_*; (3) the X-ray flux is a strongly increasing function of i; (4) 230 GHz image size is a complicated function of i, a_*, and T_i/T_e, but the $T_i/T_e = 10$ models are generally large and at most marginally consistent with the 230 GHz very long baseline interferometry (VLBI) data; (5) for models with $T_i/T_e = 10$ and $i = 85°$ the event horizon is cloaked behind a synchrotron photosphere at 230 GHz and will not be seen by VLBI, but these models overproduce near-infrared and X-ray flux; (6) in all models whose SEDs are consistent with observations, the event horizon is uncloaked at 230 GHz; (7) the models that are most consistent with the observations have $a_* \sim 0.9$. We finish with a discussion of the limitations of our model and prospects for future improvements.

Key words: accretion, accretion disks – black hole physics – Galaxy: center – MHD – radiative transfer

Online-only material: color figures

1. INTRODUCTION

Long-term studies of the stellar dynamics in the central parsec of our Galaxy indicate that the object in the center of the Milky Way is massive and compact and is therefore likely to be a supermassive black hole (BH; we will use Sgr A* to refer to the radio source, the putative BH, and the surrounding accretion flow). Recent estimates of Sgr A*'s mass $M = 4.5 \pm 0.4 \times 10^6\, M_\odot$ and distance $D = 8.4 \pm 0.4$ kpc (Ghez et al. 2008; Gillessen et al. 2009) indicate that it has the largest angular size of any known BH ($GM/(c^2 D) \simeq 5.3\ \mu$as).

Sgr A* is frequently monitored at all available wavelengths: in radio since its discovery in 1974 (Balick & Brown 1974), and more recently in submillimeter, near-infrared (NIR), and X-rays. It is heavily obscured in the optical and UV ($A_V \simeq 30$ mag). Sgr A* is a "quiescent" galactic nucleus because its bolometric luminosity in units of the Eddington luminosity is low, $L_{\rm bol} \simeq 10^{-9} L_{\rm Edd}$. The discovery of polarized emission at $\lambda = 1.3$ mm allowed the use of Faraday rotation to place a model-dependent limit on the mass accretion rate $2 \times 10^{-7} < \dot{M} < 2 \times 10^{-9}\, M_\odot$ yr^{-1} at $r < 20\, GM/c^2$ (Bower et al. 2005; Marrone et al. 2006). Submillimeter very long baseline interferometry (VLBI) of Sgr A* shows structure at very small angular scales (Doeleman et al. 2008).

Sgr A*'s spectral energy distribution (SED) can be fit with semianalytic quasispherical radiatively inefficient accretion flow (RIAF) models (e.g., Narayan et al. 1998), RIAF + outflow models (Yuan et al. 2003), and with time-dependent magnetohydrodynamics (MHD) models (e.g., Goldston et al. 2005; Ohsuga et al. 2005; Mościbrodzka et al. 2007). Other workers have modeled the VLBI and submillimeter emission (Broderick & Loeb 2005, 2006a, 2006b; Huang et al. 2007; Miyoshi et al. 2008; Broderick et al. 2009; Yuan et al. 2009) assuming a stationary RIAF or time-dependent general relativistic MHD models (Dexter et al. 2009) and computing emission at submillimeter wavelengths taking into account general relativistic effects.

In this work, we simultaneously model the SED, including Compton scattering, and the VLBI data using a relativistically self-consistent approach. We assume that accretion onto Sgr A* proceeds through a geometrically thick, optically thin, two-temperature flow that we model using a general relativistic MHD (GRMHD) simulation. BH spin a_* is self-consistently accounted for. We also assume that the (likely time-dependent, anisotropic, nonthermal) state of the plasma can be described by assigning a single temperature T_i to the ions and a possibly different temperature T_e to the electrons. Conduction is neglected.

The main goal of this work is to explore how a_*, the inclination i, and the ion-to-electron temperature ratio T_i/T_e are constrained by the data. Our paper is organized as follows. In Section 2, we review broadband observations of Sgr A*. In Section 3, we outline our technique for computing the evolution of the accretion flow and the emergent radiation. In Section 4, we present the results of single- and two-temperature SED computations and compare them to the observed SED. We summarize and discuss the model limitations in Section 5.

2. OBSERVATIONS

Sgr A* has rich observational database in radio (Serabyn et al. 1997; Falcke et al. 1998; Zhao et al. 2003; An et al. 2005; Marrone et al. 2006), NIR (Davidson et al. 1992; Herbst et al. 1993; Stolovy et al. 1996; Telesco et al. 1996; Menten et al. 1997; Melia & Falcke 2001; Hornstein et al. 2002; Genzel et al. 2003; Eckart et al. 2006; Schödel et al. 2007), X-rays (Baganoff et al. 2001, 2003; Goldwurm et al. 2003; Porquet et al. 2003; Bélanger et al. 2005, 2006; Porquet et al. 2008), and even γ-rays (Aharonian et al. 2004, but see Aharonian et al. 2008).

In general, the emission from Sgr A* in the radio band is rising with the frequency. Below $\nu = 10$ GHz the spectral slope α ($F_\nu \sim \nu^\alpha$) was found to be $\alpha \approx 0.1$[3] (Serabyn et al. 1997; Falcke et al. 1998). Between 10 and 300 GHz the spectral slope changes to $\alpha \approx 0.5$ (Falcke et al. 1998; An et al. 2005).

Marrone (2006) reported that the spectral slope becomes flat or declining between 230 GHz (1.3 mm) and 690 GHz (0.43 mm), consistent with a transition from optically thick to optically thin radiation. He estimated a variance-weighted mean value of $\alpha = -0.18$ from four observational epochs (each epoch lasting around 2 hr, and α changing from -0.46 to 0.08). The quiescent NIR counterpart of Sgr A* has been reported by Genzel et al. (2003), but it is not clear whether the "quiescent" NIR emission at the position of Sgr A* is background noise or a real detection of Sgr A* (Do et al. 2009). Thus, the measured quiescent emission in the NIR is usually interpreted as an upper limit. The quiescent luminosity at the 2–8 keV band measured with the *Chandra* observatory is $L_X = 2.4 \times 10^{33}$ erg s^{-1}, and the emission is extended with an intrinsic size of 1.″4, consistent with the Bondi radius. The mass accretion rate at the Bondi radius deduced from X-ray observations is $\sim 10^{-6}\, M_\odot$ yr^{-1} (Baganoff et al. 2003). Above the stationary emission, Sgr A* exhibits intraday variability at all observed wavelengths (flares in submillimeter, NIR, and X-rays that often rise simultaneously).

High-frequency VLBI constrains the structure of Sgr A* on angular scales comparable to $GM/(c^2 D) \simeq 5.3$ μas. The distribution of intensities on the sky is a convolution of the (wavelength-dependent) intrinsic angular structure with anisotropic interstellar broadening proportional to λ^2 (Bower et al. 2006; Doeleman et al. 2008). Sgr A* has been detected by $\lambda = 1.3$ mm VLBI on baselines between Hawaii (JCMT), Arizona (SMTO), and California (CARMA; Doeleman et al. 2008). This small number of baselines does not permit imaging of the emitting region or the "silhouette" of the BH (Bardeen 1973; Chandrasekhar 1983; Falcke et al. 2000; Takahashi 2004), but it does constrain models of the emitting region. Using a (two-parameter) symmetric Gaussian brightness distribution model, Doeleman et al. (2008) infer a full width at half maximum FWHM $= 37^{+16}_{-10}$ μas, or $\simeq 7GM/(c^2 D)$. This is *very small*, since the apparent diameter of the BH is $2\sqrt{27}GM/(c^2 D) \simeq 55$ μas. The FWHM for a Gaussian model has also been estimated at 7 mm (0.268 ± 0.025 mas, or $51GM/(c^2 D)$; Bower et al. 2004) and at 3.5 mm (0.126 ± 0.017 mas, or $28GM/(c^2 D)$; Shen et al. 2005), but longer wavelength intrinsic size is more difficult to measure because scatter broadening dominates the observed image size at $\lambda \gtrsim 1$ mm. VLBI observations at $\lambda = 0.8$ mm (345 GHz) and 0.65 mm (450 GHz) are expected in the near future (Doeleman et al. 2009).

3. MODEL

Our model consists of three parts: a physical model of the accreting plasma, a numerical realization of the physical model, and a procedure for calculating the emergent radiation from the accreting plasma.

The physical model is a geometrically thick, optically thin, turbulent plasma accreting onto a rotating BH in a statistically steady state. The angular momentum of the hole is assumed to be aligned with the angular momentum of the accreting plasma.[4] The ions and electrons are assumed to have a thermal distribution function, but with a temperature ratio T_i/T_e that may be different from one (see Section 2.2.1 in Sharma et al. 2007, for a discussion of temperature ratios in a collisionless accretion flow model; their work suggests that $T_i/T_e \sim 10$ may be a natural value). The equation of state is gas pressure $P = (\gamma - 1)u$ (where u is the proper internal energy density), with $\gamma = 13/9$, appropriate to a plasma with $\Theta_i \equiv kT_i/(m_p c^2) \ll 1$ and $\Theta_e \equiv kT_e/(m_e c^2) \gg 1$ (we will discuss our procedure for extracting an electron temperature later). The parameters of the accreting plasma model, then, are a_* and T_i/T_e.

The numerical realization of the physical model uses the GRMHD code `harm`, a conservative shock-capturing scheme with constrained transport to preserve $\nabla \cdot \mathbf{B} = 0$ (Gammie et al. 2003). All models in this paper are *axisymmetric*; we will explore three-dimensional models in a subsequent publication. Our grid is uniform in modified spherical Kerr–Schild coordinates (Gammie et al. 2003), which permit the flow to be followed through the event horizon. The coordinates are logarithmic in the Kerr–Schild radius R and nonuniform in Kerr–Schild colatitude θ (Boyer–Lindquist and Kerr–Schild R and θ are identical).[5] The resolution is 256×256.

The inner boundary of the computational domain is at $R_{\rm in} = 0.98(1 + \sqrt{1 - a_*^2})$, i.e., just inside the event horizon. The outer boundary is at $R_{\rm out} = 40\, GM/c^2 \simeq 1.8$ AU, or an angular radius of $\simeq 210$ μas. Since low-frequency emission is believed to arise at larger radius, this means that we are unable to model the low-frequency (radio and mm) portion of the SED.

We must also supply initial conditions and boundary conditions. For numerical convenience, we adopt the same initial equilibrium torus used by Gammie et al. (2003), McKinney & Gammie (2004), and others. This torus has an inner boundary at $6\, GM/c^2$ and a rest-mass density maximum $\rho_{\rm max}$ at $R_{\rm max} = 12\, GM/c^2$.[6] It is seeded with a weak, purely poloidal field that follows the isodensity contours and has minimum $\beta \equiv P/(B^2/(8\pi)) = 100$ (see Gammie et al. 2003 for details). Small perturbations are added to the internal energy. The torus quickly becomes turbulent due to the magnetorotational instability (Balbus & Hawley 1991). At $R \lesssim R_{\rm max}$ the accretion flow soon reaches a nearly (statistically) stationary state that is independent of the initial conditions (except for the magnetic field geometry; see Hawley & Krolik 2002; Beckwith et al. 2008). If our numerical model accurately represents the physical model, this inner accretion flow should be similar to the inner portion of a much more extended accretion flow. We use outflow boundary conditions at both the inner and outer boundaries, and the usual polar boundary conditions at $\theta = 0$ and $\theta = \pi$. We integrate for $2000GM/c^3 \simeq 12$ hr, or eight orbital periods at $R_{\rm max}$.

`harm` (and similar codes) fail if ρ or u are small in comparison to the kinetic and magnetic energy densities, or the density in nearby zones. To prevent this, we impose a hard "floor," so that $\rho > 10^{-4}\rho_{\rm max}(R/GM/c^2)^{-3/2}$ and $u > 10^{-6}\rho_{\rm max}c^2(R/GM/c^2)^{-5/2}$.

[3] Not to be confused with the phenomenological viscosity α of accretion disk theory. In this paper, angular momentum transport is calculated self-consistently in a GRMHD model.

[4] Tilted or "oblique" accretion flows, require three-dimensional simulations; antialigned flows can be modeled using an axisymmetric simulation, but likely provide a worse fit to the data than the low-spin aligned flows considered here.

[5] The modified Kerr–Schild coordinates x_0, x_1, x_2, x_3 are related to spherical Kerr–Schild coordinates t, R, θ, ϕ by $t = x_0$, $R = e^{x_1}$, $\theta = \pi x_2 + \frac{1}{2}(1-h)\sin(2\pi x_2)$, and $\phi = x_3$. We set $h = 0.3$.

[6] For $a_* = 0.5$, we set $R_{\rm max} = 13\, GM/c^2$ so that scale height H has $H/R_{\rm max}$ similar for all the models.

Table 1
Summary of MHD and SED for Models with $T_i/T_e = 1$

Run	a_*	i (deg)	$\langle \dot{M} \rangle$ ($10^{-9}\ M_\odot\ \mathrm{yr}^{-1}$)	α	$\log_{10} L_X$ (erg s^{-1})	η	η_{TD}	Consistent w/Obs.?
		5	3.97	−2.04	30.9	8.9×10^{-3}		No
A	0.5	45	3.55	−1.78	30.7	8.0×10^{-3}	0.0821	No
		85	3.81	−1.21	31.3	8.6×10^{-3}		No
		5	1.6	−1.94	31.1	2.4×10^{-2}		No
B	0.75	45	1.39	−1.69	31.0	2.1×10^{-2}	0.112	No
		85	1.5	−1.12	31.6	2.2×10^{-2}		No
		5	0.94	−1.92	31.3	4.8×10^{-2}		No
C	0.875	45	0.87	−1.65	31.3	4.3×10^{-2}	0.145	No
		85	0.91	−1.07	32.3	4.5×10^{-2}		No
		5	0.86	−1.67	31.9	7.1×10^{-2}		No
D	0.94	45	0.78	−1.41	32.1	6.4×10^{-2}	0.179	No
		85	0.80	−0.87	33.1	6.6×10^{-2}		No
		5	0.85	−1.51	32.3	0.11		No
E	0.97	45	0.78	−1.25	32.7	0.1	0.213	No
		85	0.80	−0.68	33.8	0.1		No
		5	0.64	−1.51	32.9	0.19		No
F	0.98 5	45	0.58	−1.25	33.1	0.17	0.245	No
		85	0.59	−0.69	34.2	0.18		No

Note. The columns from left to right are run ID, dimensionless spin of the BH, inclination angle of the observer with respect to the BH spin axis, averaged rest-mass accretion rate, α spectral slope between 230 and 690 GHz ($F \sim \nu^\alpha$), and luminosity in the X-rays (at $\nu \sim 10^{18}$ Hz), the radiative efficiency $\eta = L_{\mathrm{BOL}}/\dot{M}c^2$, the thin-disk efficiency for the same a_*, and whether the model is consistent with the data.

To "observe" the numerical model, we must specify the observer's distance D and the inclination i of the BH spin to the line of sight. Because the dynamical simulation is scale free but the radiative transfer calculation is not, we need to specify the simulation length unit $\mathcal{L} = GM/c^2$, time unit $\mathcal{T} = GM/c^3$, and mass unit $\mathcal{M}$ (equivalently, the mass accretion rate). Since we set the peak density in the GRMHD model to 1 in simulation units, the peak density is $\mathcal{M}/\mathcal{L}^3$ in cgs units. The mass unit is *not* set by M (which appears in the dynamical model only in the combination GM) because the flow mass is $\ll M$, and has negligible effect on the gravitational field. $\mathcal{M}$ is therefore a free parameter.

To calculate the SED, we use the relativistic Monte Carlo scheme `grmonty`. A detailed description of the algorithm and tests is given in Dolence et al. (2009). The code fully accounts for synchrotron emission and absorption, and Compton scattering. It uses a "stationary flow" approximation, computing the spectrum through each time slice of simulation data as if it were time independent. This is an approximation because the light crossing time is comparable to the dynamical time. It is done because tracking photons through the time-dependent simulation data is still too computationally expensive. We will evaluate the quality of this approximation once we are able to calculate fully self-consistent spectra. An average spectrum is formed by averaging over 50 single slice spectra from each of four different realizations of the simulation (the realizations differ in the random number seed used to generate initial conditions).

To image the model, we use the relativistic ray-tracing code `ibothros`, which accounts only for synchrotron emission and absorption, again using a stationary flow approximation (see Noble et al. 2007). An average image is created using the same averaging procedure as for the spectra.

To sum up, the model parameters (aside from those that describe the initial conditions) are M, D, i, a_*, T_i/T_e, and $\mathcal{M}$. M and D are set by the observations of stellar orbits; we briefly explore the consequence of varying them below. $\mathcal{M}$ we will set for each model by requiring that time-averaged flux $F_\nu(230\ \mathrm{GHz}) = 3.4$ Jy. The remaining three free parameters are a_*, i, and T_i/T_e.

In what follows we explore models with $a_* = 1 - 2^{-n}$, with $n = 1, 2, 3, 4, 5,$ and 6, i.e., $a_* \approx 0.5, 0.75, 0.88, 0.94, 0.97,$ and 0.98, $T_i/T_e = 1$, 3, and 10, and $i = 5°$, 45°, and 85°.

The observational constraints on the model are (aside from the 230 GHz flux density) the submillimeter spectral slope α, the upper limit on the quiescent NIR flux density (Genzel et al. 2003; Melia & Falcke 2001; Hornstein et al. 2002; Schödel et al. 2007; Dodds-Eden et al. 2009), and the upper limit on the quiescent luminosity between 2 and 8 keV (Baganoff et al. 2003). Since the measured L_X is produced inside 1.″4 ($\approx 10^5\ GM/c^2$), and our simulation domain covers only the inner 40 GM/c^2, we exclude models for which L_X is close to the "quiescent emission" L_X.[7]

4. RESULTS

We have studied the combinations of model parameters listed in Table 1 ($T_i/T_e = 1$), Table 2 ($T_i/T_e = 3$), and Table 3 ($T_i/T_e = 10$). The model that best satisfies the observational constraints has $a_* = 0.94$ (model D), $T_i/T_e = 3$, and $i = 85°$. We will present this "best-bet" model in some detail before going on to the full parameter survey (see Section 4.2) to give the reader a physical sense for the models.

4.1. Best-bet Model

In what follows, we will consider time, and realization averaged SEDs and images. But to get a sense for physical conditions in the accretion flow, consider a single time slice at $t = 1680\ GM/c^3$. Figure 1 shows the run of n_e, B^2, and Θ_e

[7] We use the source brightness profile (Baganoff et al. 2003) and estimate that 50% of the X-ray luminosity comes from the central pixel of size 0.″492. This is still far larger than our computational domain, so we require that the X-ray luminosity in our models should not exceed $L_X = 1.2 \times 10^{33}$ erg s^{-1}.

Table 2
Summary of MHD and SED for Models with $T_i/T_e = 3$

Run	a_*	i (deg)	$\langle \dot{M} \rangle$ ($10^{-9}\ M_\odot\ \mathrm{yr}^{-1}$)	α	$\log_{10} L_X$ (erg s^{-1})	η	η_{TD}	Consistent w/ Obs.?
		5	10.0	−2.09	30.5	3.4×10^{-3}		No
A	0.5	45	8.8	−1.72	32.4	3.1×10^{-3}	0.0821	No
		85	10.7	−0.75	31.3	3.6×10^{-3}		No
		5	3.9	−1.99	31.0	9.5×10^{-3}		No
B	0.75	45	3.5	−1.59	31.0	8.5×10^{-3}	0.112	No
		85	4.1	−0.67	31.7	9.9×10^{-3}		No
		5	2.28	−1.97	31.1	2.0×10^{-2}		No
C	0.875	45	2.07	−1.54	31.2	1.8×10^{-2}	0.145	No
		85	2.43	−0.56	32.3	2.1×10^{-2}		No
		5	1.9	−1.68	31.5	3.5×10^{-2}		No
D	0.94	45	1.7	−1.27	31.8	3.1×10^{-2}	0.179	No
		85	1.86	−0.44	32.9	3.4×10^{-2}		Yes
		5	1.86	−1.37	32.2	6.0×10^{-2}		No
E	0.97	45	1.68	−1.01	32.5	5.4×10^{-2}	0.213	No
		85	1.83	−0.21	33.8	5.9×10^{-2}		No
		5	1.4	−1.48	32.6	0.11		No
F	0.98	45	1.23	−1.13	32.9	0.10	0.245	No
		85	1.29	−0.26	34.3	0.10		No

Note. Columns same as in Table 1.

Table 3
Summary of MHD and SED for Models with $T_i/T_e = 10$

Run	a_*	i (deg)	$\langle \dot{M} \rangle$ ($10^{-9}\ M_\odot\ \mathrm{yr}^{-1}$)	α	$\log_{10} L_X$ (erg s^{-1})	η	η_{TD}	Consistent w/Obs.?
		5	90.8	−1.37	30.1	5.4×10^{-4}		No
A	0.5	45	117.1	−0.2	31.4	6.7×10^{-4}	0.0821	Yes
		85	369.0	1.38	33.5	1.6×10^{-3}		No
		5	38.3	−1.05	30.0	1.6×10^{-3}		No
B	0.75	45	50.2	0.04	31.8	2.0×10^{-3}	0.112	Yes
		85	190.6	1.49	34.6	6.9×10^{-3}		No
		5	19.5	−1.15	31.4	5.1×10^{-3}		No
C	0.875	45	23.6	−0.07	32.0	6.2×10^{-3}	0.145	Yes
		85	41.4	1.19	34.2	1.7×10^{-2}		No
		5	13.7	−0.93	31.8	1.1×10^{-2}		No
D	0.94	45	15.2	−0.05	32.3	1.1×10^{-2}	0.179	Yes
		85	31.2	1.17	34.4	2.5×10^{-2}		No
		5	13.6	−0.40	32.5	2.6×10^{-2}		Yes
E	0.97	45	14.3	0.2	33.1	2.8×10^{-2}	0.213	No
		85	26.5	1.19	35.2	5.1×10^{-2}		No
		5	9.07	−0.6	32.7	5.3×10^{-2}		Yes
F	0.98	45	9.16	−0.08	33.2	5.2×10^{-2}	0.245	No
		85	15.5	1.12	35.4	9.0×10^{-2}		No

Note. Columns same as in Table 1.

in the time slice. Evidently, 10^7 cm^{-3} is a typical equatorial plane density, 30 G is a typical field strength, and $\Theta_e = 10$ is a typical electron temperature. Note that the field changes from a tangled, turbulent structure near the midplane to a more organized structure in the "funnel" over the poles of the BH. Temperature generally increases away from the midplane.

In Figure 2, we show the SED computed from the same time slice used in Figure 1 (thick line) along with the average SED (thin line). The figure also shows a selection of radio, NIR, and X-ray observational data points (references given in the figure caption). The SED has a peak at ∼690 GHz due to thermal synchrotron emission. Below ∼100 GHz it fails to fit the data because that emission is produced outside the simulation volume. A second peak in the far UV is due to the first Compton scattering order, and at $\gtrsim 10^{19}$ Hz ($\gtrsim$40 keV) the photons are produced by two or more scatterings.

Where do the photons originate in each band? Figure 3 maps the points of origin for photons in the synchrotron peak (230–690 GHz), in the NIR (2–10 μm), and in the X-ray (2–8 keV). Most of the submillimeter emission originates near the midplane at $4\ GM/c^2 < r < 6\ GM/c^2$. NIR photons are produced in hot regions with high magnetic field intensity and high gas temperature, and these are concentrated close to the innermost stable circular orbit (ISCO; $r_{\rm ISCO} \approx 2\ GM/c^2$ for $a_* = 0.94$), i.e., they come from between $2\ GM/c^2 < r < 6\ GM/c^2$. All photons responsible for the formation of the first Compton bump are upscattered between $2\ GM/c^2 < r < 8\ GM/c^2$ but the 2–8 keV emission is produced mainly by scatterings in the hottest

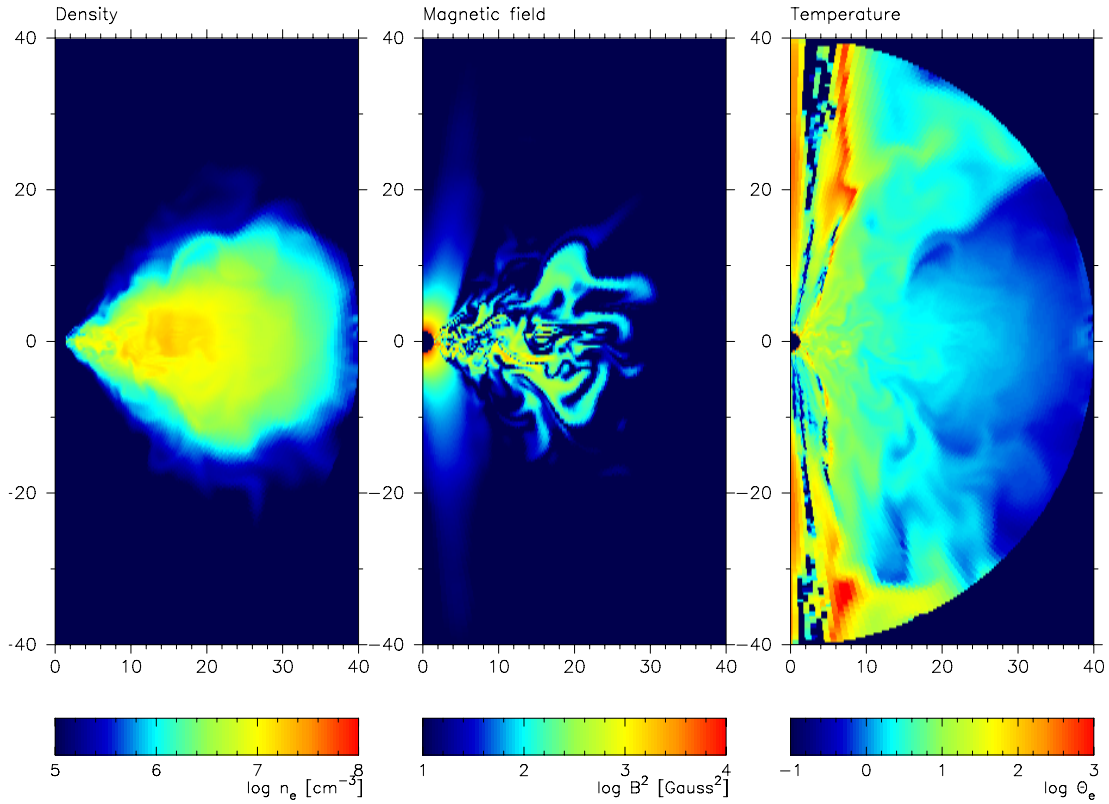

Figure 1. Disk structure in our best-bet model with $a_* = 0.94$ (model D) and with $T_i/T_e = 3$. The number density, the magnetic field strength, and the electron temperature are shown in the left, middle, and right panels, respectively. The axis scale units are GM/c^2. The figure presents a single time slice.
(A color version of this figure is available in the online journal.)

parts of the disk at $2\ GM/c^2 < r < 3\ GM/c^2$. Emission can be seen around the borders of the funnel in each panel, but this is at a low level and is associated with unreliable temperatures assigned by `harm` to the funnel region.

The photons that form the submillimeter peak (690 GHz) originate at $\langle r \rangle \approx 4\ GM/c^2$, where $\langle n_e \rangle \approx 4 \times 10^6$ cm^{-3} $\langle B \rangle \approx 28$ G, and $\langle \Theta_e \rangle \approx 17$.[8] The emissivity $\nu j_\nu(\theta = \pi/2)$ calculated from these averaged values peaks at $\nu \sim 8 \times 10^{11}$ Hz, which is quite close to the actual peak in νL_ν (where $\nu L_\nu = 4\pi D^2 \nu F_\nu$). The averaged values also yield $B^2/(8\pi P) \simeq 0.25$; the submillimeter peak plasma is dominated by gas pressure rather than magnetic pressure.

The optically thin synchrotron photons in the energy range between the synchrotron peak and first-order Compton scattering bump ($6.9 \times 10^{11} < \nu < 1.5 \times 10^{14}$ Hz) tend to arise in current sheets at $2\ GM/c^2 < r < 6\ GM/c^2$, where $1.5 < n_e/(10^6\ \text{cm}^{-3}) < 4$, $\langle B \rangle = 30$–35 G, and $\Theta_e \approx 80$ or higher. The corresponding νj_ν peaks in the mid-IR, at 12 μm. These current sheets have higher entropy than the surrounding plasma, consistent with the idea that they are heated by (numerical) reconnection. The prominence of the current sheets is likely an artifact of axisymmetry. Similar current sheets are seen in axisymmetric shearing box models of disks that are not present in three-dimensional shearing box models.[9]

The synchrotron photons Compton scatter at $2\ GM/c^2 < r < 8\ GM/c^2$ where $16 < \Theta_e < 70$. The X-ray emission at

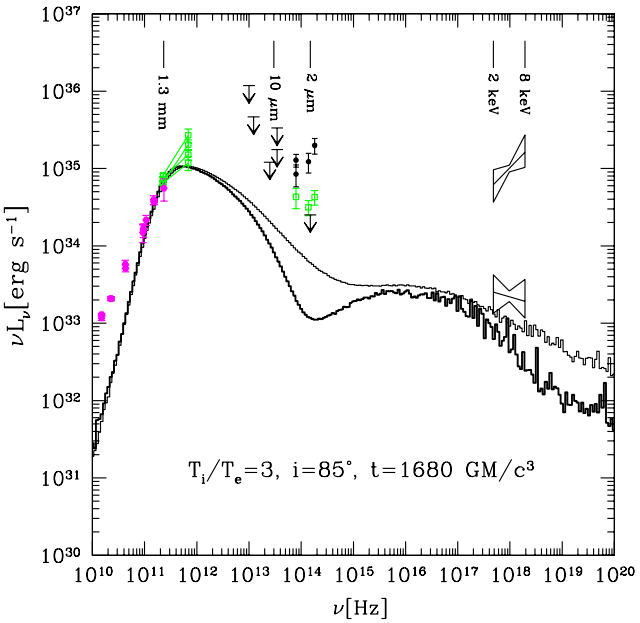

Figure 2. SEDs computed based on a single time slice $t = 1680\ GM/c^3$ (thick line) (see Figure 1 for the distributions of the physical variables corresponding to the same time) along with the time-averaged spectrum (thin line) of our best-bet model. Observational points are taken from: Falcke et al. (1998); An et al. (2005); Marrone et al. (2006) at radio, Genzel et al. 2003 at NIR (1.65, 2.16, and 3.76 μm), and Baganoff et al. 2003 at X-rays (2–8 keV). The upper limits in the NIR band are taken from Melia & Falcke (2001) (30, 24.5 and 8.6 μm), Schödel et al. (2007) (8.6 μm) and Hornstein et al. (2007) (2 μm). The points in the NIR at flaring state are from Genzel et al. (2003) (1.65, 2.16, and 3.76 μm), and Dodds-Eden et al. (2009) (3.8 μm). An example of X-ray flare ($L_X = 1 \times 10^{35}$ erg s^{-1}) is taken from Baganoff et al. (2001).
(A color version of this figure is available in the online journal.)

[8] Angle brackets indicate an average over grid zones weighted with the photon number "detected" in a given frequency band.

[9] Our best guess is that well-resolved three-dimensional models will exhibit heating that is more evenly distributed. Direct, physical heating of the electrons can take place in this strongly shearing region via plasma instabilities acting on anisotropic pressure, as discussed by Sharma et al. (2007).

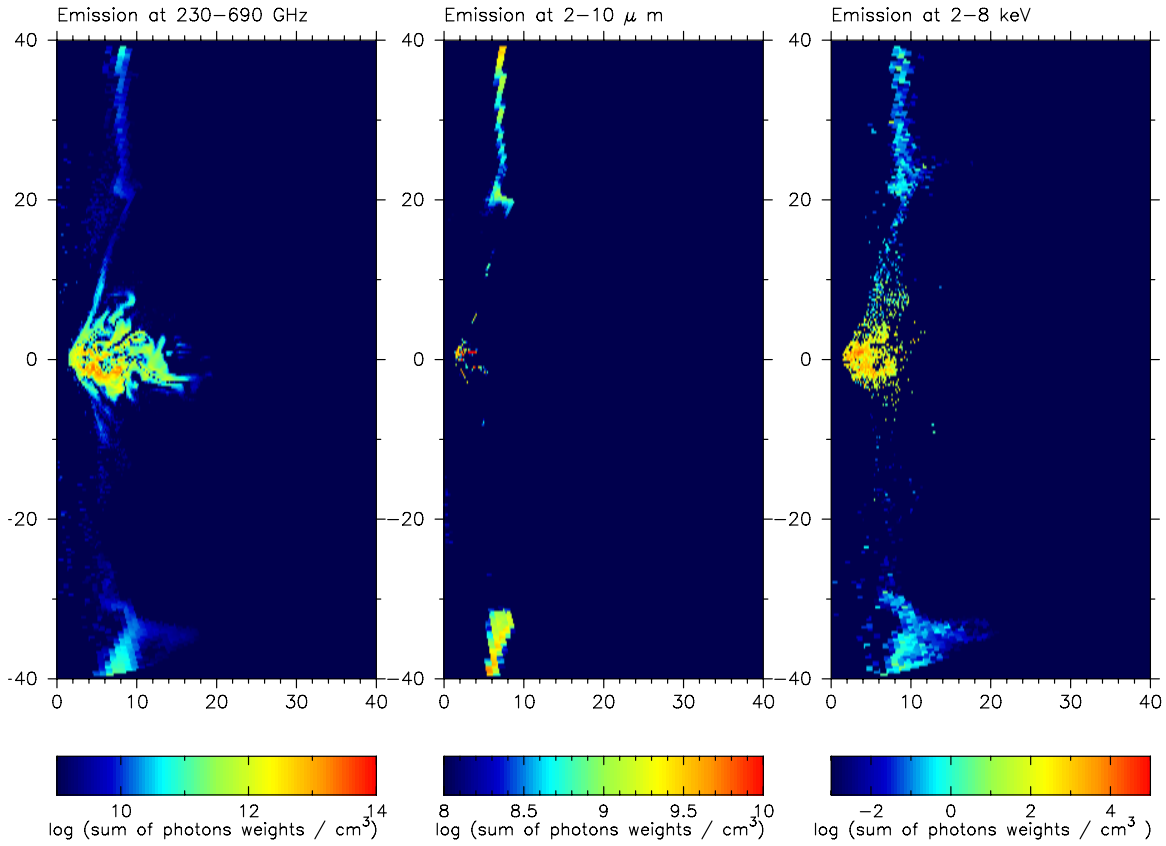

Figure 3. Maps showing the point of origin for photons in our best-bet model. We show the logarithm of the sum of the photon weights in each zone, which is proportional to the number of photons seen at 230–690 GHz (left), 2–10 μm (middle), and 2–8 keV (right) bands. The axis scale units are GM/c^2. The figure presents a single time slice at $t = 1680\ GM/c^3$. Note that color bands differ in scales.

(A color version of this figure is available in the online journal.)

2–8 keV is formed by scatterings from the plasma with $\langle\Theta_e\rangle = 35$ at $\langle r\rangle = 3\ GM/c^2$. For this temperature, the average energy amplification per scattering is $1 + 4\Theta_e + 16\Theta_e^2 \approx 1.9 \times 10^4$, consistent with the seed photons with energies $2.5 \times 10^{13} < \nu < 10^{14}$ Hz (11 μm $> \lambda >$ 2.9 μm). This means that many of the seed photons are produced in current sheets, and so some uncertainty attaches to the Compton scattered flux. We know observationally that Sgr A* produces frequent flares with fluxes larger than those produced by our quiescent-source model, so there is a source of seed photons in this energy band, albeit a fluctuating one.

A small fraction of photons are emitted from the funnel wall at large radii (15–40 GM/c^2) where the gas temperature is $\Theta_e \sim 10^3$. This is also likely an artifact of the inability of `harm` and similar codes to track the internal energy of a fluid when the internal energy is much smaller than the other energy density scales. Nevertheless, this raises the interesting question of what the electron distribution function *should* be in the funnel. High-energy electrons might be naturally generated within this tenuous plasma by steepening of MHD waves excited by turbulence near the equatorial plane.

4.2. Parameter Survey

In Figure 4, we present averaged spectra for models with different spins (referred to as A, B, C, D, E, and F; see Tables 1–3), inclination angles $i = 85°$, 45°, and 5° in the upper, middle, and bottom panels, respectively, and temperature ratio $T_i/T_e = 1$, 3, and 10 from left to right. All SEDs are averaged over time and runs as described in Section 3.

The tables indicate whether the model is consistent with observations. The model can fail in one of the four ways: it can produce the wrong submillimeter spectral slope α, it can overproduce the quiescent NIR flux, it can overproduce the quiescent X-ray flux, and it can be too large at 230 GHz to be consistent with the VLBI data. The last constraint we will discuss separately in the following section. It may be useful to recall that $\mathcal{M}$ is adjusted in each model so that the 230 GHz flux is 3.4 Jy.

The model can also fail by cooling too rapidly to be consistent with our neglect of cooling in the dynamical model. The tables list a radiative efficiency $\eta \equiv L_{\rm BOL}/\dot{M}c^2$, where $L_{\rm BOL}$ is the bolometric luminosity (integrated over the solid angle), and for comparison a thin-disk efficiency at the same a_*. η ranges between 5.4×10^{-4} for $a_* = 0.5$, $T_i/T_e = 10$ and 0.18 for $a_* = 0.98$, $T_i/T_e = 1$ (the thin-disk efficiency for the latter is 0.25). Only in the $a_* = 0.98$, $T_i/T_e = 1$ model is the radiative efficiency sufficiently high that cooling is likely to have a significant effect on the GRMHD model. We will consider models with cooling in a future publication.

Very few of the time-averaged SEDs based on a single-temperature ($T_i/T_e = 1$) models produce the correct α. The exception is edge-on tori ($i = 85°$) around fast spinning BHs (models E and F). These models are ruled out, however, because they overproduce NIR and X-ray flux.

For $T_i/T_e = 3$, only the model with $a_* = 0.94$ seen at $i = 85°$ agrees with the data. This is the best-bet model discussed in Section 4.1. For $i = 85°$, models with spins below $a_* = 0.94$ (A, B, and C) are ruled out by the inconsistent spectral slope,

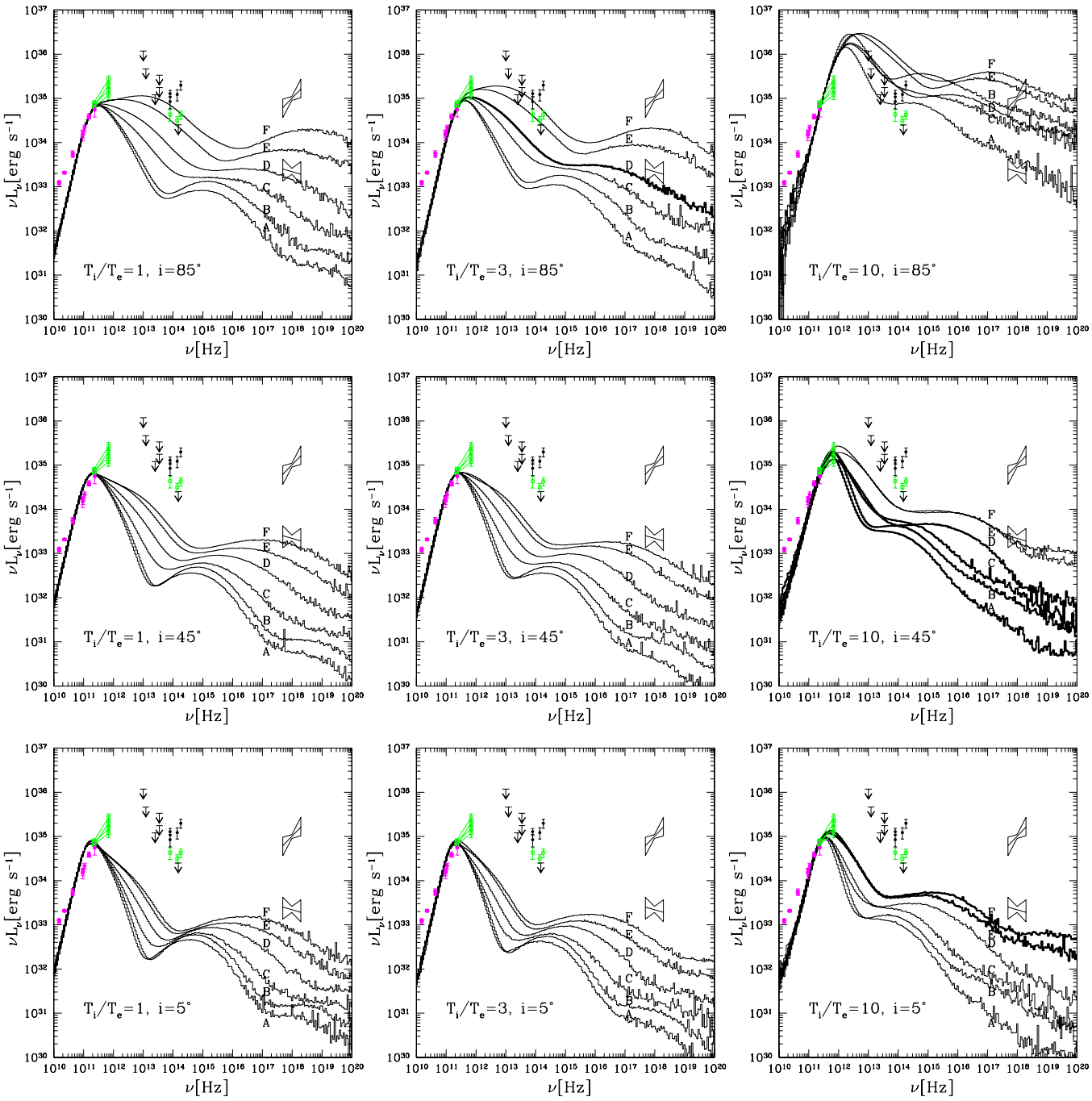

Figure 4. SEDs computed for $T_i/T_e = 1, 3$, and 10 in left, middle, and right panels, respectively, and $i = 5°, 45°$, and $85°$ in the bottom, middle, and top panels, respectively. Models A, B, C, D, E, and F have different a_* (see Tables 1–3). Each SED is a result of averaging over 200 individual SEDs taken from last 500 GM/c^3 of the GRMHD runs (4 runs and 50 dumps for each spin). Observational points and upper limits as in Figure 2. Models consistent with the observations are marked with thick lines.

(A color version of this figure is available in the online journal.)

and models with higher spins (E and F), although consistent with the observed α, overproduce the quiescent NIR and X-ray emission. All models with $T_i/T_e = 3$ observed at $i = 5°$ and $45°$ are ruled out by the inconsistent α.

For $T_i/T_e = 10$, we find that all models with $i = 85°$ are ruled out by both α and violation of NIR and X-ray limits. For lower inclination angles ($i = 5°, 45°$) a few models (E and F with $i = 5°$, and A, B, C, and D at $i = 45°$) reproduce the observed α. These models are consistent with X-rays and NIR limitations. Models E and F for $i = 45°$ are ruled out by NIR and X-ray limitations whereas models A, B, C, and D for $i = 5°$ produce α which is too small.

What is the physical origin of these constraints?

The dependence on a_* arises largely because as a_* increases the inner edge of the disk—the ISCO—reaches deeper into the gravitational potential of the BH, where the temperature and magnetic field strength are higher. In the disk midplane, the temperature is a fraction of the virial temperature and scales with radius $\Theta_e \propto 1/r$. $B \propto 1/r$, while the density $\sim r$, below the pressure maximum. Holding all else constant (which we

Table 4
The Size of the Emitting Region at 230 GHz

Run	a_*	i	$T_i/T_e = 1$		$T_i/T_e = 3$		$T_i/T_e = 10$	
			σ_1	σ_2	σ_1	σ_2	σ_1	σ_2
		5	41.7	41.6	38.1	38.0	35.9	35.9
A	0.5	45	31.2	28.4	28.9	25.9	32.7	31.6
		85	23.1	20.7	23.3	21.9	37.6	33.9
		5	38.8	38.7	35.4	35.3	34.6	34.6
B	0.75	45	28.6	25.9	26.7	23.7	31.2	30.2
		85	20.7	19.4	20.8	20.4	36.9	32.3
		5	39.3	39.2	35.2	35.0	31.9	31.8
C	0.875	45	29.3	26.7	26.4	23.4	29.3	28.0
		85	20.6	19.4	20.4	19.7	30.6	30.1
		5	37.2	37.1	32.2	32.1	28.0	28.0
D	0.94	45	27.4	25.3	24.0	21.5	24.7	23.9
		85	19.2	18.4	18.5	17.2	27.1	26.4
		5	37.0	36.9	31.2	31.1	26.5	26.4
E	0.97	45	27.4	25.7	23.4	21.6	23.6	23.4
		84	19.6	18.2	18.1	17.3	25.8	24.6
		5	36.5	36.4	31.3	31.2	26.1	26.1
F	0.98	45	27.2	25.2	23.4	21.2	22.8	21.7
		85	18.8	18.4	16.5	17.6	23.8	22.6

Notes. The columns from left to right are: run ID, dimensionless spin of the black hole (BH), inclination angle i, size of the emitting region in terms of standard deviation in the major (σ_1) and the minor (σ_2) axis for $T_i/T_e = 1$ (Columns 4 and 5), $T_i/T_e = 3$ (Columns 6 and 7), and $T_i/T_e = 10$ (Columns 8 and 9) in units of μas. For a Gaussian model, the VLBI data require FWHM$= 37^{+16}_{-10}$ μas(Doeleman et al. 2008), or $\sigma = 16^{+6.8}_{-4.2}$ μas.

do not; we hold the 230 GHz flux constant) this implies a higher peak frequency for synchrotron emission, a constant Thomson depth (in our models, the Thomson depth at the ISCO is roughly constant, since the path length $1/ \sim r_{\rm ISCO}$ but the density $\sim r_{\rm ISCO}$), and a larger energy boost per scattering $A \approx 16\Theta_e^2$, as can be seen in comparing models with different spins in Figure 4. The X-ray flux therefore increases with a_* because Θ_e at the ISCO increases.

The dependence on T_i/T_e is mainly due to synchrotron self-absorption, which is strongest at high inclination. For example, because the $i = 85^\circ$, $T_i/T_e = 10$ model is optically thick at 230 GHz, the emission is produced in a synchrotron photosphere well outside $r_{\rm ISCO}$. The typical radius of the synchrotron photosphere ranges between 15 GM/c^2 for low-spin models ($a_* = 0.5, 0.75$) and 8 GM/c^2 for high-spin models ($a_* > 0.75$). The 230 GHz flux can then be produced only with large $\mathcal{M}$; as $\mathcal{M}$ increases the optically thin flux in the NIR increases due to increasing density and field strength. The scattered spectrum also depends on T_i/T_e since the energy boost per scattering is $\sim 16\Theta_e^2 \propto 1/(T_i/T_e)^2$.

The inclination dependence is, interestingly, a relativistic effect. $\mathcal{M}$ is nearly independent of i (it varies by $\sim$10%, except for $T_i/T_e = 10$, which due to optical depth effects has much larger variation), so models with different inclination are nearly identical. Nevertheless, the X-ray flux varies dramatically with i, increasing by almost 2 orders of magnitude from $i = 5^\circ$ to $i = 85^\circ$. This occurs because Compton-scattered photons are beamed forward parallel to the orbital motion of the disk gas. The variation of mm flux with i is due to self-absorption. The mm flux reflects the temperature and size of the synchrotron photosphere. At lower i, the visible synchrotron photosphere is hotter than at high i.

There is an additional constraint due to Faraday rotation measurements, but this constraint is qualitatively different because we do not directly calculate Faraday rotation in our model. Instead we adopt the constraints on $\dot{M}$ which are inferred, via a separate model, from the Faraday rotation data (Bower et al. 2005; Marrone et al. 2006). $\dot{M}$ increases, in a nonlinear way, with increasing T_i/T_e. For $T_i/T_e = 1$, $\dot{M} > 6 \times 10^{-10}\, M_\odot$ yr^{-1}. For $T_i/T_e = 10$, $\dot{M} < 4 \times 10^{-7}\, M_\odot$ yr^{-1}. All these values are consistent with the Faraday rotation constraints, although the highest $\dot{M}$, $T_i/T_e = 10$, models are only marginally consistent.

There are a few other general trends worth mentioning. In all models, the average optical depth drops below 1 at 0.4–1.3 mm. For $i > 45^\circ$ and high BH spins $a_* > 0.75$ the emission in the NIR band (2 μm) is formed by the direct synchrotron emission while the 2–8 keV emission results from a first-order scattering. For low BH spins $a_* \leqslant 0.75$, the emission in NIR is due to first-order Compton scatterings, and the X-ray is second-order scattering. For $T_i/T_e = 10$ and $i = 5^\circ$ independently of the BH spin the NIR emission is formed by a first-order Compton scatterings and X-rays by second-order scatterings.

4.3. Images and the Size of the Emitting Region

We compute the 230 GHz intensity maps of our models using a ray-tracing code (Noble et al. 2007) and we average them in the same manner as the spectra. To estimate the size of the emitting region, we calculate the eigenvalues of the matrix formed by taking the second angular moments of the image on the sky (i.e., the length of the "principal axes"). The eigenvalues along the major (σ_1) and the minor (σ_2) axis are given in Table 4. In Figure 5, we show averaged 230 GHz images for models with SEDs that are consistent with the data.

The source size depends on the model parameters. For $i > 45^\circ$, we find a critical mass accretion rate $\dot{M} \approx 10^{-8}\, M_\odot$ yr^{-1} (the exact value depends on a_* and i) below which the size of the emitting region decreases monotonically with increasing T_i/T_e. Above $\dot{M} \approx 10^{-8}\, M_\odot$ yr^{-1}, the size of the emitting region increases with increasing T_i/T_e. The increasing trend can be explained by the appearance of the synchrotron photosphere at 230 GHz for larger mass accretion rates at high inclination. For $i = 85^\circ$ and $T_i/T_e = 10$, at 230 GHz the BH horizon is cloaked by the photosphere and cannot be observed by VLBI (note that this model is ruled out for other reasons). For a constant T_i/T_e and i, the size always decreases with increasing a_*, because the emissivity of the central regions increases with a_*.

The size of the emitting region for our best-bet model is consistent with the observed FWHM $= 37$ μas (inferred from VLBI data using a two-parameter Gaussian model). For $T_i/T_e = 10$, the sizes of the images are inconsistent with the VLBI measurement, except model D, which is only marginally consistent. Note that this moment-based analysis is crude. It would be better to "observe" the model with the same baselines used in gathering the VLBI data (this would add a new parameter, the position angle). Our analysis is particularly ill suited to low i models that are ringlike and therefore poorly fit by a Gaussian model.

4.4. Varying Distance and Mass

In our discussion, we have fixed the mass and distance of Sgr A*, but these are uncertain to $\sim$5%. How would changing these parameters change our results?

First, consider how $\mathcal{M}$ depends on M and D. Near the sub-millimeter peak, $F_\nu \propto n_e B \mathcal{L}^3 D^{-2} \sim \mathcal{M}^{3/2}\mathcal{L}^{-1/2}\mathcal{T}^{-1} D^{-2} \sim (\mathcal{M}/M)^{3/2} D^{-2}$ (since $\mathcal{L} \sim M$ and $\mathcal{T} \sim M$) *if* the model is optically thin (although there are usually optically thick lines

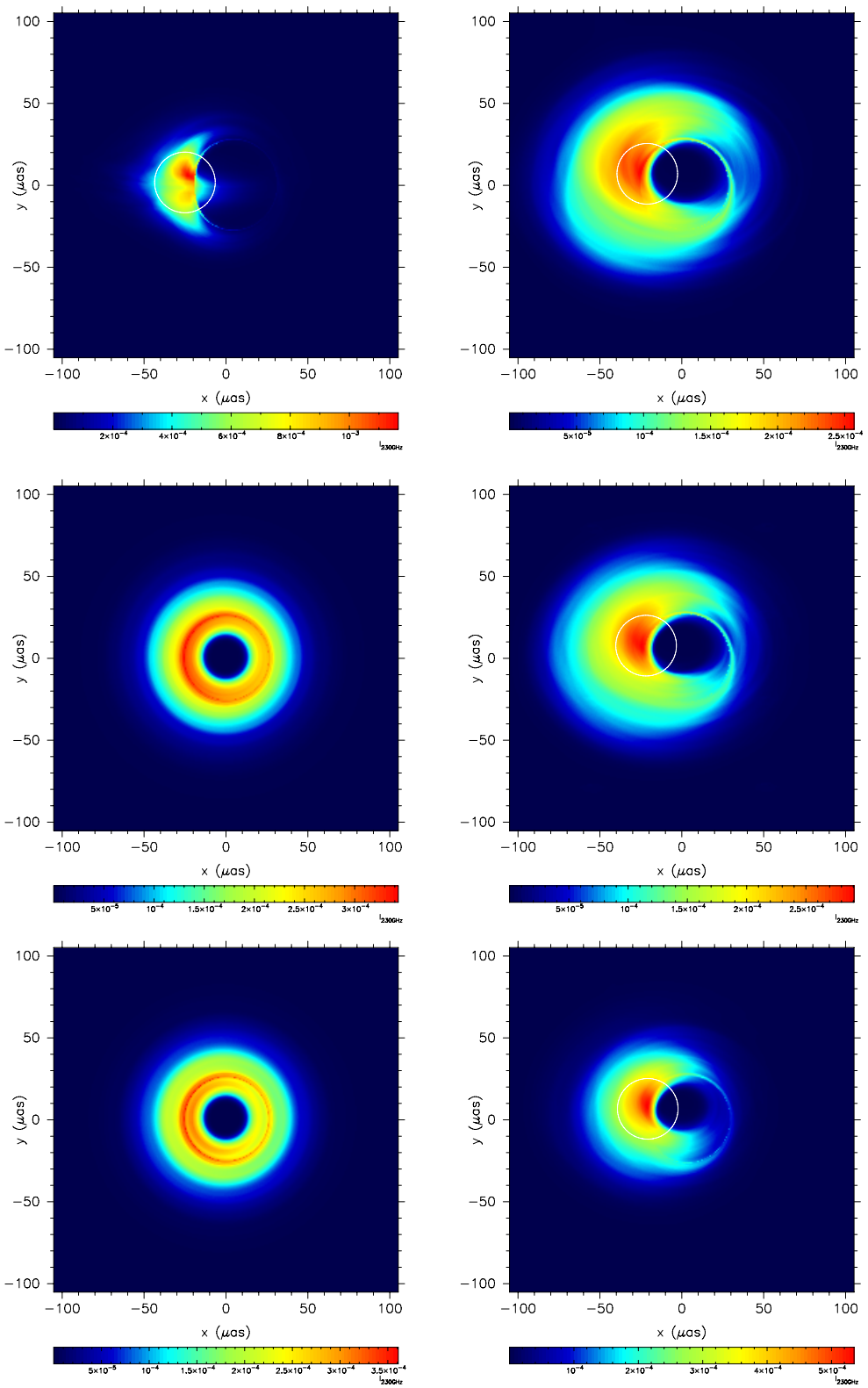

Figure 5. Images of the accretion flow at 230 GHz for models with SEDs that are consistent with observations of Sgr A*. The images has been averaged over time and over four separate realizations of each model. Intensities are given in units of erg s^{-1} pixelsize^{-2} Hz^{-1} sr^{-1}, where the pixel size is 0.82 μas. The images show inner 40 GM/c^2. Left top panel shows model D with $T_i/T_e = 3$ at $i = 85°$. Left middle and bottom panels show high-spin models E and F, respectively, for $T_i/T_e = 10$ and $i = 5°$. The right panels show models A, B, and D for $T_i/T_e = 10$ and $i = 45°$ in the upper, middle, and lower panels, respectively. The white circle marks FWHM = 37 μas of a symmetric Gaussian brightness profile centered at the image centroid.

(A color version of this figure is available in the online journal.)

of sight through the model even if the mean optical depth at the submillimeter peak is < 1). We therefore expect that $\mathcal{M} \sim D^{4/3}M$.

Consider varying M and D in our best-bet model (model D; $T_i/T_e = 3$ and $i = 85°$). We find that $\Delta\mathcal{M}/\mathcal{M} \approx 15\%$ when changing the distance from 8.0 kpc to 8.8 kpc if we fix

$M = 4.5 \times 10^6\, M_\odot$. In particular, $\mathcal{M} = 17.5 \times 10^{18}$, 18.9×10^{18}, 20.6×10^{18} for $D = 8.0$, 8.4, and 8.8 kpc, respectively. For $D = 8.4$ kpc, $\mathcal{M} = 18.2 \times 10^{18}$, 18.9×10^{18}, and 20.6×10^{18} for $M = 4.1$, 4.5, and $4.9 \times 10^6\, M_\odot$, respectively, which gives $\Delta\mathcal{M}/\mathcal{M} \approx 10\%$ when changing BH mass from 4.1 to $4.8 \times 10^6\, M_\odot$. This is crudely consistent with our expectations based on an optically thin source.

Finally, we change the mass and distance simultaneously according to the observational relation $M D^{-1.8} =$ constant (Ghez et al. 2008). For $D = 8.0$ kpc and $M = 4.1 \times 10^6\, M_\odot$, $\mathcal{M} = 16.6 \times 10^{18}$ whereas for $D = 8.8$ kpc and $M = 4.8 \times 10^6\, M_\odot$, $\mathcal{M} = 20.4 \times 10^{18}$. We find that at $D = 8.0$ kpc, $M = 4.1 \times 10^6\, M_\odot$, $\alpha = -0.32$, $\log_{10} L_X = 33.0$; at $D = 8.4$ kpc, $M = 4.5 \times 10^6\, M_\odot\, \alpha = -0.44$, $\log_{10} L_X = 32.9$; at $D = 8.8$ kpc, $M = 4.8 \times 10^6\, M_\odot$, $\alpha = -0.47$, $\log_{10} L_X = 32.7$. The spectral slope and X-ray luminosity therefore vary $< 25\%$.

Our best-bet model remains consistent with the data, then, if we vary with M and D within the range permitted by observation. Models with $T_i/T_e = 10$ and $i = 45^\circ$ with BH spin $a_* = 0.97$ and 0.98 become acceptable if M and D are lowered, but only the model with $a_* = 0.98$ would be (marginally) consistent with VLBI measurements of the Sgr A*size. In sum, D and M are tightly constrained; varying them within the narrow range of values permitted by observations does not change the main conclusions of this work.

5. SUMMARY

Under the assumption that the accretion flow at the galactic center is optically thin, geometrically thick, and lightly magnetized, we have presented constraints on a_*, T_i/T_e, and i for Sgr A*. We find that models with $T_i/T_e = 3$ and 10 describe the sub-mm spectral observations (α) better than models with $T_i/T_e = 1$. We find that the model with $T_i/T_e = 3$, BH spin $a_* \approx 0.94$ and the close to edge-on inclination angles is consistent with the broadband SED observational data and the size of Sgr A* measured by VLBI. In this case the silhouette of the BH is difficult to observe because Doppler boosting of the disk emission places almost all the emission on one side of the BH.

If, on the other hand, the electrons are heated relatively inefficiently ($T_i/T_e = 10$) then models with $a_* = 0.97, 0.98$ observed at $i = 5^\circ$, or $a_* = 0.5, 0.75, 0.88, 0.94$ observed at $i = 45^\circ$ are consistent with the observed SED. The sizes of the emitting regions in these models, however, seem to be inconsistent with the VLBI measurements, except again at $a_* = 0.94$.

Our best-bet estimate of the BH spin ($a_* = 0.94$) disagrees with Broderick et al. (2009) (following Yuan et al. 2009) who found $a_* = 0^{+0.4}$ and $i = 90^\circ_{-50^\circ}$ (2σ errors) based on a careful analysis of images of RIAF models. The discrepancy may be a consequence of different emissivity (ours is based on P. K. Leung et al. 2009, in preparation), and different underlying models for the run of temperature, density profile, magnetic field strength, and geometry of the flow. We also do not include nonthermal emission as in Broderick et al. (2009). The results for $T_i/T_e = 10$ and $i = 45^\circ$ at low-spin values agree with the previous study, but according to our moment analysis these models are inconsistent with the VLBI data. An analysis of images at $\nu = 230$ GHz that folds the models through the VLBI observation process is needed to definitely exclude models based on the VLBI data.

Our a_* and i constraints are different from those presented in Noble et al. (2007), because here we allow $T_i/T_e \neq 1$. We do not find a good fit to the observational data for single-temperature models which were studied in the earlier work. We confirm the trend that the bolometric luminosity increases with the increasing BH spin.

The models studied here differ in many respects from those considered earlier by Mościbrodzka et al. (2007). The earlier models were based on low angular momentum, nonrelativistic hydrodynamic models for the accretion flow that extended over a wide range in radii. The models described here are fully relativistic MHD models that extend over a limited range in radius and use fully relativistic radiative transfer.

There are still significant uncertainties in our models. These uncertainties fall into four categories: the unimportant, those which may be important and easily be eliminated with a small additional effort, those which may be important and require a major effort, but are in principle straightforward to eliminate, and those which are serious and require new physical understanding.

In the interests of full disclosure, our unimportant approximations are (1) we use a γ law equation of state rather than a Synge-type equation of state that would more accurately represent our two-temperature relativistic gas. H. Shiokawa et al. (2009, in preparation) show that the associated changes in spectra are small; (2) for $T_i/T_e \gtrsim 10$ our cyclo-synchrotron emissivity and absorptivity are imperfect because most of the emission comes from electrons with $\Theta_e \sim 1$, where our approximate expression begins to break down (P. K. Leung et al. 2009, in preparation);[10] (3) we neglect bremsstrahlung, which is expected to be important only far from the horizon; (4) we neglect double Compton scattering. The cross section for the double Compton process is $\sim e^2/\hbar c$ (fine-structure constant) smaller than single Compton scattering and can be neglected here (also $h\nu \ll m_e c^2$); (5) we neglect induced Compton scattering. Induced Compton scattering is important for $(k_B T_b/m_e c^2)\tau_T \gtrsim 1$, where T_b is the brightness temperature. In Sgr A* $T_b \approx 10^{10}$ K and $\tau_T \ll 1$ so it is indeed negligible.

The significant approximations that could be fixed with some additional effort include: (1) our neglect of cooling; it is straightforward to run our GRMHD models with cooling, but then they are no longer scale free. With cooling turned on we would need to fix $\mathcal{M}$ by evolving the GRMHD model at a trial $\mathcal{M}$, calculating the spectrum, and repeating until $F_\nu(230\ \mathrm{GHz}) = 3.4$ Jy. (2) Axisymmetry, three-dimensional models are available but far more expensive to evolve. Use of a three-dimensional models would permit us to evolve models with (3) a wider range of radii, so that millimeter emission could be included and even the submillimeter emission could be more accurately modeled. We have not run axisymmetric models with radially extended accretion flows because they tend to develop pathologies (strong, radially extended magnetic filaments). (4) Our neglect of nonthermal electrons. These could readily be included using a phenomenological prescription for the shape and amplitude of the nonthermal portion of the electron distribution function (Özel et al. 2000; Yuan et al. 2003; Chan et al. 2009), (5) our use of the steady-state approximation in calculating SEDs and images. This would require time-dependent radiative transfer, which is straightforward in principle but computationally expensive.

[10] For models with $T_i/T_e = 1$ and 3, the error in SED associated with our approximate emissivity function is less than 1% at all frequencies. For $T_i/T_e = 10$ the errors are less than 10% at 230 GHz because the emissivity-weighted mean temperature is lower and self-absorption is important. The errors are taken from comparison of the P. K. Leung et al. (2009, in preparation) emissivity formula with directly integrated cyclo-synchrotron harmonics for lowest values of Θ_e found in our simulations.

Other approximations can be fixed only with significant additional effort: (1) our neglect of pair production. This would require a model for the radiation field near the pair production threshold. Our preliminary estimates suggest that in many of our models pair production is substantial. One advantage of incorporating pair production is that it might permit us to eliminate our numerical floor and therefore more accurately evolve the low-density funnel region; (2) our treatment of thermal energy in the funnel. `harm` tends to produce high temperatures in the tenuous funnel plasma, some of which are clearly numerical artifacts caused by application of the density floor and other, more subtle, numerical issues associated with the small ratio of thermal energy density to other energy densities; (3) our simplistic, two-temperature thermal model for the plasma. This includes our neglect of conduction and anisotropy of the plasma.

New physical understanding would be required to predictively model (1) nonthermal parts of the distribution function and (2) the initial magnetic field configuration. Nonthermal particles can of course be included in a phenomenological prescription, but the particle injection and acceleration processes are still not fully understand. As we have already mentioned, prior work shows that the GRMHD models depend nontrivially on the initial field configuration. We have adopted a simple, numerically appealing initial configuration, but the long-term evolution of the large-scale field is ill understood.

Finally, note that there are observational constraints from polarization data and from light curves (statistically, the one- and two-point statistics of the light curves at each frequency, and the cross-correlations between different frequencies). Treating the polarization data requires accurate emissivities and absorptivities, as well as models that extend well past the radius where $\Theta_e = 1$, which is where most of the intrinsic Faraday rotation occurs. The light curves require full, time-dependent radiative transfer, since the dynamical time is comparable to the light crossing time.

This work was supported by the National Science Foundation under grants AST 00-93091, PHY 02-05155, and AST 07-09246, through TeraGrid resources provided by NCSA and TACC, and by a Richard and Margaret Romano Professorial scholarship, a Sony faculty fellowship, and a University Scholar appointment to CFG. The authors are grateful to Stu Shapiro, Fred Lamb, Dan Marrone, Shep Doeleman, and Vincent Fish for discussion and comments.

REFERENCES

Aharonian, F., et al. 2004, A&A, 425, L13
Aharonian, F., et al. 2008, A&A, 492, L25
An, T., Goss, W. M., Zhao, J.-H., Hong, X. Y., Roy, S., Rao, A. P., & Shen, Z.-Q. 2005, ApJ, 634, L49
Baganoff, F. K., et al. 2001, Nature, 413, 45
Baganoff, F. K., et al. 2003, ApJ, 591, 891
Balbus, S. A., & Hawley, J. F. 1991, ApJ, 376, 214
Balick, B., & Brown, R. L. 1974, ApJ, 194, 265
Bardeen, J. M. 1973, in Black Holes (Les Astres Occlus), ed. C. DeWitt & B. S. DeWitt (New York: Gordon and Breach), 215
Beckwith, K., Hawley, J. F., & Krolik, J. H. 2008, ApJ, 678, 1180
Bélanger, G., Goldwurm, A., Melia, F., Ferrando, P., Grosso, N., Porquet, D., Warwick, R., & Yusef-Zadeh, F. 2005, ApJ, 635, 1095
Bélanger, G., et al. 2006, ApJ, 636, 275
Bower, G. C., Falcke, H., Herrnstein, R. M., Zhao, J.-H., Goss, W. M., & Backer, D. C. 2004, Science, 304, 704
Bower, G. C., Falcke, H., Wright, M. C., & Backer, D. C. 2005, ApJ, 618, L29
Bower, G. C., Goss, W. M., Falcke, H., Backer, D. C., & Lithwick, Y. 2006, ApJ, 648, L127
Broderick, A. E., Fish, V. L., Doeleman, S. S., & Loeb, A. 2009, ApJ, 697, 45
Broderick, A. E., & Loeb, A. 2005, MNRAS, 363, 353
Broderick, A. E., & Loeb, A. 2006a, ApJ, 636, L109
Broderick, A. E., & Loeb, A. 2006b, MNRAS, 367, 905
Chan, C.-K., Liu, S., Fryer, C. L., Psaltis, D., Özel, F., Rockefeller, G., & Melia, F. 2009, ApJ, 701, 521
Chandrasekhar, S. (ed.) 1983, in Int. Ser. Monographs on Physics 69, The Mathematical Theory of Black Holes (Oxford: Clarendon), 663
Davidson, J. A., Werner, M. W., Wu, X., Lester, D. F., Harvey, P. M., Joy, M., & Morris, M. 1992, ApJ, 387, 189
Dexter, J., Agol, E., & Fragile, P. C. 2009, ApJ, 703, 142
Do, T., Ghez, A. M., Morris, M. R., Yelda, S., Meyer, L., Lu, J. R., Hornstein, S. D., & Matthews, K. 2009, ApJ, 691, 1021
Dodds-Eden, K., et al. 2009, ApJ, 698, 676
Doeleman, S., et al. 2009, Astro2010: The Astronomy and Astrophysics Decadal Survey Science White Papers, no. 68
Doeleman, S. S., et al. 2008, Nature, 455, 78
Dolence, J. C., Gammie, C. F., Mościbrodzka, M., & Leung, P. 2009, ApJS, 184, 387
Eckart, A., et al. 2006, A&A, 450, 535
Falcke, H., Goss, W. M., Matsuo, H., Teuben, P., Zhao, J.-H., & Zylka, R. 1998, ApJ, 499, 731
Falcke, H., Melia, F., & Agol, E. 2000, ApJ, 528, L13
Gammie, C. F., McKinney, J. C., & Tóth, G. 2003, ApJ, 589, 444
Genzel, R., Schödel, R., Ott, T., Eckart, A., Alexander, T., Lacombe, F., Rouan, D., & Aschenbach, B. 2003, Nature, 425, 934
Ghez, A. M., et al. 2008, ApJ, 689, 1044
Gillessen, S., Eisenhauer, F., Trippe, S., Alexander, T., Genzel, R., Martins, F., & Ott, T. 2009, ApJ, 692, 1075
Goldston, J. E., Quataert, E., & Igumenshchev, I. V. 2005, ApJ, 621, 785
Goldwurm, A., Brion, E., Goldoni, P., Ferrando, P., Daigne, F., Decourchelle, A., Warwick, R. S., & Predehl, P. 2003, ApJ, 584, 751
Hawley, J. F., & Krolik, J. H. 2002, ApJ, 566, 164
Herbst, T. M., Beckwith, S. V. W., & Shure, M. 1993, ApJ, 411, L21
Hornstein, S. D., Ghez, A. M., Tanner, A., Morris, M., Becklin, E. E., & Wizinowich, P. 2002, ApJ, 577, L9
Hornstein, S. D., Matthews, K., Ghez, A. M., Lu, J. R., Morris, M., Becklin, E. E., Rafelski, M., & Baganoff, F. K. 2007, ApJ, 667, 900
Huang, L., Cai, M., Shen, Z.-Q., & Yuan, F. 2007, MNRAS, 379, 833
Marrone, D. P. 2006, PhD thesis, Harvard Univ.
Marrone, D. P., Moran, J. M., Zhao, J.-H., & Rao, R. 2006, J. Phys. Conf. Ser., 54, 354
McKinney, J. C., & Gammie, C. F. 2004, ApJ, 611, 977
Melia, F., & Falcke, H. 2001, ARA&A, 39, 309
Menten, K. M., Reid, M. J., Eckart, A., & Genzel, R. 1997, ApJ, 475, L111
Miyoshi, M., Kameno, S., Ishituka, J. K., Shen, Z.-Q., Takahashi, R., & Horiuchi, S. 2008, arXiv:0809.3548
Mościbrodzka, M., Proga, D., Czerny, B., & Siemiginowska, A. 2007, A&A, 474, 1
Narayan, R., Mahadevan, R., Grindlay, J. E., Popham, R. G., & Gammie, C. 1998, ApJ, 492, 554
Noble, S. C., Leung, P. K., Gammie, C. F., & Book, L. G. 2007, Class. Quantum Grav., 24, 259
Ohsuga, K., Kato, Y., & Mineshige, S. 2005, ApJ, 627, 782
Özel, F., Psaltis, D., & Narayan, R. 2000, ApJ, 541, 234
Porquet, D., Predehl, P., Aschenbach, B., Grosso, N., Goldwurm, A., Goldoni, P., Warwick, R. S., & Decourchelle, A. 2003, A&A, 407, L17
Porquet, D., et al. 2008, A&A, 488, 549
Schödel, R., Eckart, A., Mužić, K., Meyer, L., Viehmann, T., & Bower, G. C. 2007, A&A, 462, L1
Serabyn, E., Carlstrom, J., Lay, O., Lis, D. C., Hunter, T. R., & Lacy, J. H. 1997, ApJ, 490, L77
Sharma, P., Quataert, E., Hammett, G. W., & Stone, J. M. 2007, ApJ, 667, 714
Shen, Z.-Q., Lo, K. Y., Liang, M.-C., Ho, P. T. P., & Zhao, J.-H. 2005, Nature, 438, 62
Stolovy, S. R., Hayward, T. L., & Herter, T. 1996, ApJ, 470, L45
Takahashi, R. 2004, ApJ, 611, 996
Telesco, C. M., Davidson, J. A., & Werner, M. W. 1996, ApJ, 456, 541
Yuan, F., Quataert, E., & Narayan, R. 2003, ApJ, 598, 301
Yuan, Y. -F., Cao, X., Huang, L., & Shen, Z.-Q. 2009, ApJ, 699, 722
Zhao, J.-H., Young, K. H., Herrnstein, R. M., Ho, P. T. P., Tsutsumi, T., Lo, K. Y., Goss, W. M., & Bower, G. C. 2003, ApJ, 586, L29